CANADIAN JOURNAL OF EXPLORATION GEOPHYSICS
VOL. 28, NO. 2 (DECEMBER 1992), P 96-108

MECHANICS OF UNDERWATER SOUND FROM A PULSED PLASMA JET

R.D. SMITH[1], R.D. WARREN[2], R.M. CLEMENTS[2] AND D.R. TOPHAM[3]

ABSTRACT

The acoustic pulse produced from a plasma jet has been investigated both theoretically and experimentally. Optical measurements of the time history of the radius of the gas bubble produced by the jet discharge have been used in conjunction with straightforward hydrodynamic theory to produce an expected pressure pulse. This compares favourably with the actual measured pulse. Results are presented having primary pulse half-widths ranging between 100 μs and 250 μs, with pulse repetition rates of up to 0.5 Hz. Specifically, both theory and experiment show that the parameters of the electrical circuit which stores the energy control the width (i.e., frequency content) of the primary pressure pulse. In addition, for a given depth the bubble pulse period is controlled by the stored energy. The theory presented here is expected to be applicable to other types of electrical discharge acoustic sources. Actual subbottom profiles for a conveniently available pinger and the plasma jet are presented.

INTRODUCTION

There is a wide variety of acoustic sources of interest for water-bottom and subbottom profiling. Each source has its own characteristic signature, characteristic with respect to both the amplitude and the frequency spectrum of the pressure pulse. This characteristic of the source is strongly linked to the source's usefulness and is thus worthy of study on its own merit. In fact, ideally, one wishes not only to understand the source's characteristic signature but also to be able to control it.

McGee et al. (1992) have compared the signature of four high-resolution seismic sources (Boomer-O.R.E. Geopulse Model 5810B, Chip Sonar-Datasonics Model TTV-160 sleeve gun-Texas Instruments S.G.I. and Plasma Gun) with the objective of assessing the digitization rates necessary for an adequate representation of the signals. This comparison of their peak frequencies and potential resolution shows that the plasma gun described by Pitt et al. (1988) compares favourably in terms of resolution.

Here, the characteristics of the pulsed plasma jet signature/pressure pulse, Smith et al. (1987) and Pitt et al. (1988), are examined over a wider range of operating conditions. It is shown that the spectral content of the pressure pulse can be controlled to some extent by the proper selection of the electrical components.

This study reports the following:

a) measurement of pressure signatures in the near field in an acoustic test facility;
b) photographic and video imaging, using shadowgraph optics, of the vapour bubble which produces the pressure pulse;
c) development of a simple theoretical model based on the experimental measurements.

EXPERIMENTAL EQUIPMENT

Underwater plasma jet source

Figure 1 schematically shows the underwater plasma jet used in this investigation. This system is fabricated of metal and is approximately 1.5 m in length. Gas (air) in the cavity is maintained by pressurizing the entire system slightly above ambient pressure and the annular space between the insulator and the central electrode provides the conduit for the piping system into the cavity. Typically, the cavity dimensions are 3-6 mm diameter and 6-10 mm length. Air flow into the cavity is only a few millilitres per second.

To break down the plasma cavity a high voltage capacitance discharge circuit is switched to a pulse transformer. A

Manuscript received by the Editor September 23, 1992; revised manuscript received January 19, 1993.

[1]Presently, Department of Physics and Astronomy, University of Victoria, Victoria, British Columbia V8W 2Y2; permanent address, Butte College, 3536 Campus Drive, Oroville, California 95965, USA

[2]Department of Physics and Astronomy, University of Victoria, Victoria, British Columbia V8W 2Y2

[3]Institute of Ocean Sciences, P.O. Box 6000, Sidney, British Columbia V8L 4B2

The authors would like to thank P.R. Smy and R.F. Haley of the University of Alberta for the use of the Spin Physics® video system. Also, the assistance of Terra Surveys Ltd. in obtaining the subbottom profiles is gratefully acknowledged. This work was supported by the Natural Sciences and Engineering Research Council of Canada (NSERC) and the University of Victoria.

high-voltage (30 kV) pulse across the central electrode and the end plate electrode causes the gases in the cavity to ionize creating a conducting path. Electrical energy stored in a capacitor bank (50-400 μF) at 500-2000 V can then discharge through the cavity producing a fully developed arc. An inductor (13-51 μH) isolates the breakdown circuit from the discharge circuit. In operation the electrical system behaves as a series RLC circuit with a variable resistance. Thus, control of the frequency of the circuit is possible by changing the capacitance and/or the inductance of the circuit. Circuit details are contained in Pitt et al. (1988).

Near field acoustic pressure measurements

A cylindrical tank 2.4 m diameter by 2.4 m high filled with fresh water was used to measure the near-field pressure signature of the underwater plasma jet discharge. Pressure was measured using an EDO 6166 calibrated hydrophone (0.02 MPa/V, 0 to 100 kHz) placed at 120 or 130 mm directly in front of the plasma cavity. This arrangement allowed approximately 1.5 ms of time before wall and surface reflections began to confuse the pressure signature. Even after 1.5 ms, spherical spreading reduced the reflections to approximately 5 percent of the direct signal. The pressure signatures were captured by a Tektronix 7D20 digital oscilloscope and recorded on a computer system.

To determine the directional characteristics of the source, two EDO 6166 calibrated hydrophones, one fixed at a known distance from centre, the other movable both in the radial and polar directions, were deployed in the same horizontal plane as the plasma gun. Circuit parameters for the experiment were C = 300 μF, L = 51 μH, V_0 = 800 V, stored energy 96 J. Because there is some shot-to-shot variation in the pressure signature of the plasma gun, the ratio of the maximum pressure of the movable hydrophone to the maximum pressure of the fixed hydrophone was used to monitor any abnormal pressure signatures during the measurement. Sound pressure levels were then calculated using eight averaged pressure values for each position. The positions of the receiving hydrophones were arranged so wall, bottom and surface reflections did not confuse the primary pressure pulse until well after the maximum pressure was reached. Measurements were made in the polar direction from -10° through 190°, 0° being straight in front of the plasma gun. Symmetry in the polar direction was assumed for the values from 190° to 360°.

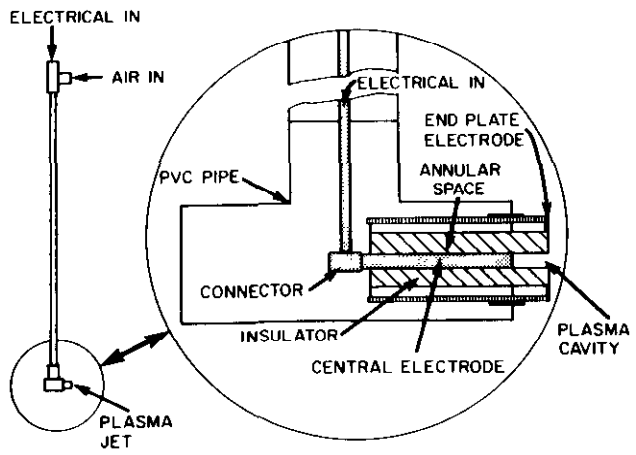

Fig. 1. Schematic diagram showing design of underwater plasma jet.

Imaging equipment

Two separate visual imaging systems were necessary to adequately image the underwater plasma discharge. Most images were made using a Spin Physics® video system capable of recording images every 250 μs. The intense light of the plasma discharge together with its electromagnetic pulse generally made imaging impossible for approximately the first millisecond after the discharge. All video images were made using a shadowgraph optical system. Density differences between the vapour produced by the plasma system and the surrounding water are successfully imaged in this way. Prior to the first millisecond of video images, streak photographs of the luminous vapour bubble were recorded using a High Spin® rotating prism drum camera. This camera recorded the expanding bubble on film at the rate of 1.3 mm/μs. Data were obtained from the two imaging systems from separate discharges with identical electrical parameters.

Both video and photographic imaging were recorded in a small transparent plastic enclosure which was too small to allow for simultaneous recording of pressure signatures.

Experimental Results

Figure 2 shows a series of video images produced by a single underwater discharge at a depth of 20 cm. It should be noted that the first two or three images after ignition are obliterated by the electromagnetic pulse. The first reasonable image is thus approximately 750 μs after ignition and the sequence documents the expansion and subsequent collapse of the vapour bubble. The first frame of the second expansion phase is marked on the figure and shows a two-phase jet of fine bubbles rather than a coherent bubble. Later in time, the fine bubbles are projected away from the source as a vortex ring structure.

The peak initial pressure produced by the underwater plasma jet depends upon the stored energy and the discharge period of the circuit. These in turn depend on the capacitance, the inductance and the applied voltage of the electrical circuit in the manner of an RLC overdamped electrical circuit. The bubble period (time from first maximum to second maximum pressure) depends only on the total stored electrical energy for a given source depth. As with a small explosion, the bubble period depends approximately upon the cube root of the total energy discharged into the water (which itself is proportional to the total stored electrical energy), Arons et al. (1948).

Figure 3(a) shows the results of the measurements of peak pressure when the movable hydrophone was at a distance of 0.711 m from the plasma gun tip. Figure 3(b) shows the results of a similar set of measurements with the movable

hydrophone at a distance of 0.356 m from the plasma gun. Note the significant notch in the pressure pattern directly behind the body of the plasma gun device, caused by the plasma gun structure shadow. At the larger distance the notch is not apparent.

The Theoretical Model

In the following model of the plasma gun, a distinction is drawn between the discharge characteristics of the electrical circuit and the physical processes accompanying the energy

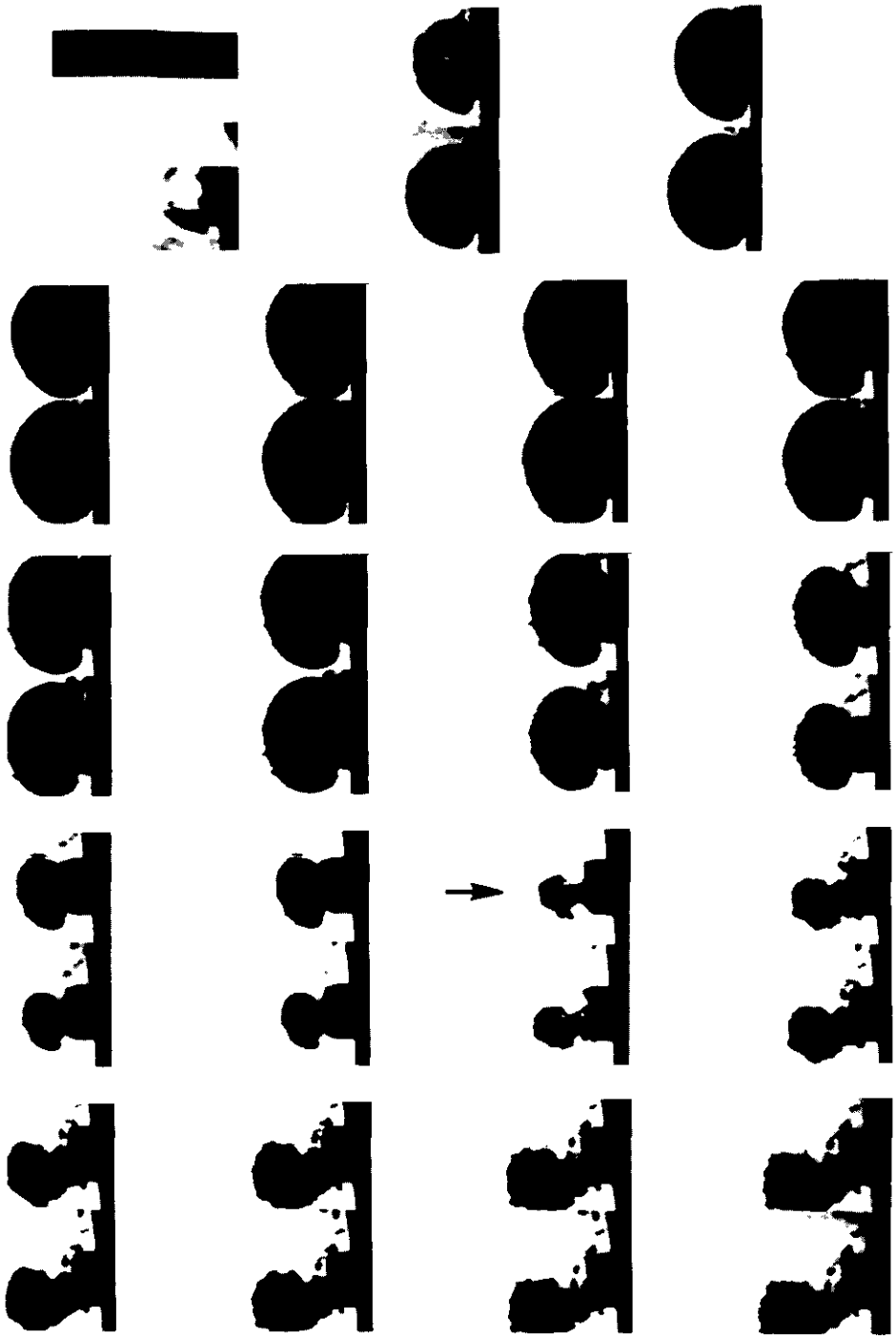

Fig. 2. Shadowgraph video images of an underwater plasma jet discharge. The storage capacitor is 200 μF charged to 1000 V with a circuit inductance of 13 μH. Each image is produced 250 μs after the preceding one; time increases top to bottom within each pair of images and then left to right.

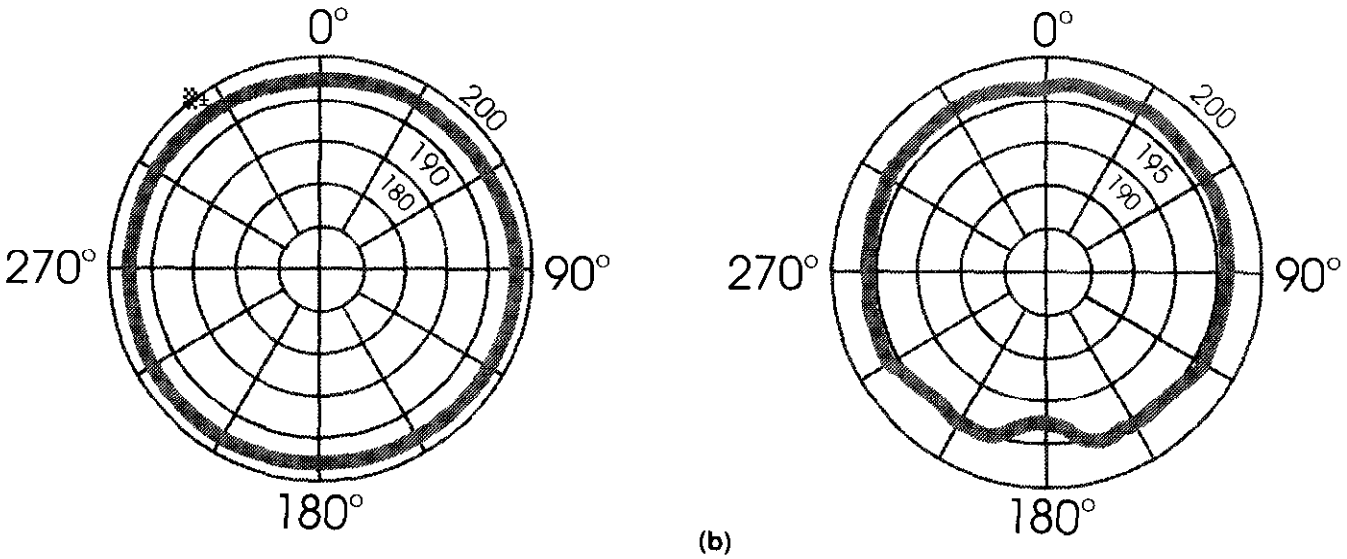

Fig. 3. Polar plot of sound pressure level (dB re 1 μPa at 1 m) measured at **a**) 0.711 m and **b**) 0.356 m.

transfer to the ambient environment. In fact, the two are coupled via the potential gradient along the arc discharge column. The decoupling is affected through an appeal to empirical matching. The circuit behaves as a series R-L-C system whose resistance changes during the discharge period. In addition to the nominal component values, this particular circuit possesses inherent capacitance and inductance of 34 μF and 11 μH, respectively. The arc discharge characteristics produce a single current pulse whose duration decreases with increasing charging voltage. The ratio of pulse width to the nominal half-period is largely a function of the charging voltage, as shown in Figure 4. These circuit characteristics have been taken into account in the theoretical calculations employed to determine the empirical matching constants for the energy transfer mechanism.

The primary mechanism for the generation of acoustic energy by such impulsive systems as the plasma gun, conventional spark sources and explosives lies in the production of a rapidly expanding gas vapour bubble. The relationship between the bubble expansion and the pressure rise induced in the water at a distance r from the centre of a sphere is given by the Rayleigh bubble equation, Lamb (1945):

$$p - p_0 = \rho\left\{\frac{R}{r}\left[R\frac{d^2R}{dt^2} + 2\left(\frac{dR}{dt}\right)^2\right] - \frac{1}{2}\left(\frac{R^2}{r^2}\frac{dR}{dt}\right)^2\right\}, \quad (1)$$

where p is the local pressure, p_0 and ρ the ambient water pressure and density and R the bubble radius. This has been extended by Keller and Kolodner (1956) to include the energy loss by acoustic radiation.

In the case of the plasma gun, three distinct phases of the pressure production can be identified: the initial breakdown within the cavity, the period of heat addition, and the subsequent bubble expansion and collapse. The initial breakdown

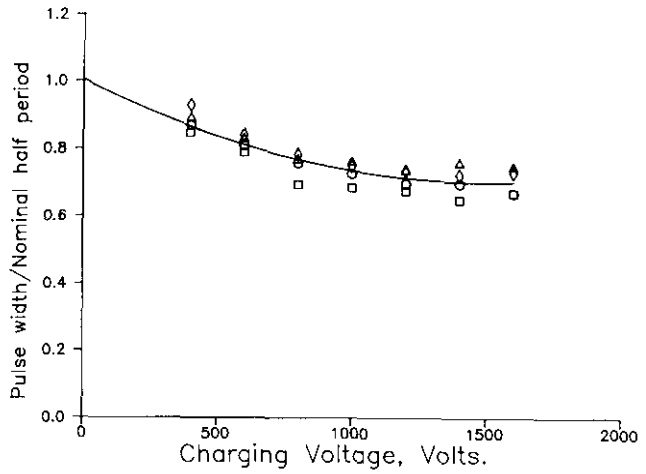

Fig. 4. Variation of discharge period with charging voltage. Circuit parameters are: circles 100 μF, 13 μH; squares 100 μF, 51 μH; triangles 200 μF, 13 μH; diamonds 200 μF, 51 μH.

and expansion to fill the arc cavity can be modelled following the methods of Topham (1971, 1972) and Cowley (1974). This shows that the arc column expands to fill the cavity within 20 μs of initiation which is not significant for the primary pressure production.

The major mechanism to be considered for primary pressure production is the addition of mass to the expanding bubble by evaporation from the gas/water interface by heat transfer from the electrically heated plasma. This can be modelled by application of a simple gas law, supplemented by some empirical observations. Since the process of mass addition takes place by evaporation, it is assumed to be approximately isothermal in nature. The perfect gas law then gives the pressure as

$$p(t) \propto \frac{m(t)}{V(t)}, \tag{2}$$

where $m(t)$ is the instantaneous mass of gas within a bubble of volume $V(t)$ at a constant temperature.

A preliminary assessment of the performance of the plasma gun suggested that a fixed proportion of the stored energy was ultimately transferred into evaporated mass, based on the observation that the bubble period (peak-to-peak) was proportional to the cube root of the stored energy, as reported by Cole (1948) for small explosive charges. This result is extended by assuming that a fixed proportion of the instantaneous power dissipation is applied as evaporation. The mass production can then be written as

$$m(t) = \frac{\alpha}{L}\int_0^t I\, V_e\, dt, \tag{3}$$

where α is the efficiency of transfer, L the latent heat, I the instantaneous current and V_e the arc voltage. Taking a sinusoidal current waveform $I = I_0 \sin \omega t$, and scaling the arc voltage by a representative value, for example, the peak value ΔV, the power integral can be written as

$$\int_0^t I\, V_e\, dt = \frac{I_0 \Delta V}{\omega}\int_0^{\omega t} \sin \omega t \left(\frac{V_e}{\Delta V}\right) d\omega t. \tag{4}$$

Assuming that the arc voltage waveforms are geometrically similar, $V_e / \Delta V = f(\omega t)$, the power dissipated during a half period, Δt, can be written as

$$\int_0^t I\, V_e\, dt = \frac{I_0 \Delta V \Delta t}{\pi}\int_0^{\omega t} \sin \omega t\ f(\omega t) d\omega t,\ \omega t \le \pi. \tag{5}$$

In practice, the arc voltage waveform is highly variable from shot to shot and, in this circumstance, the adoption of an overall scaling similarity is the best that can be achieved. Measurements from actual waveforms give a linear relationship between $I_0 \Delta V \Delta t$ and the stored energy. The choice of the function $f(\omega t)$ partly determines the distribution of the dissipation over the cycle, so a number of simple analytical functions were tried and the resulting pressure waveforms compared with the experimental measurements. Of these, a simple sinusoidal function gave the best match to the measured pressure pulse, i.e., $f(\omega t) = \sin \omega t$.

Adopting this function, equation (5) can be integrated as

$$\int_0^t I\, V_e\, dt = \frac{I_0 \Delta V \Delta t}{2\pi}\left(\omega t - \frac{\sin 2\omega t}{2}\right),\ \omega t \le \pi.$$

Taking the factor $I_0 \Delta V \Delta t$ to be proportional to the stored energy, the above result can be substituted into equation (3) to give the mass addition as

$$m(t) = \frac{K}{L}\left(\frac{1}{2} C V_0^2\right)\left(\omega t - \frac{\sin 2\omega t}{2}\right),\ \omega t \le \pi, \tag{6}$$

where the various constant factors have been absorbed into K, the overall constant of proportionality. The efficiency of the energy transfer α has been taken as constant.

The remaining quantity to be determined is the volume dependence $V(t)$, and in principle this, together with the resulting pressure dependence, can be obtained from the solution of the Rayleigh bubble equation (1) with the mass input (6) as the forcing function. In practice, the solution is sensitive to the choice of an initial radius and requires careful "tuning" to achieve acceptable results. Here, a more robust approach based on empirical observations of the bubble radius with time over the discharge period is adopted. Measurements by Smith (1990), Arsentev (1965) and Stewart and Baird (1980) for the plasma gun, sparkers and small explosives show that the resulting bubble expands at nearly constant velocity during the discharge period and can be represented by the linear relationship,

$$R(t) = R_0 + vt \tag{7}$$

where v is the rate of expansion.

The Rayleigh equation (1) can be adopted to derive the expected functional dependence of the velocity v on the parameters of the discharge. At the surface of the bubble, $r = R$ and equation (1) reduces to

$$\frac{p(t) - p_0}{\rho} = \frac{R d^2 R}{dt^2} + \frac{3}{2}\left(\frac{dR}{dt}\right)^2. \tag{8}$$

The assumption of isothermal evaporation gives

$$\frac{p(t)}{p_0} = \frac{m(t)}{m_0}\left(\frac{R_0}{R}\right)^3,$$

where the subscript zero denotes an initial condition.

Combining this with the mass production equation (6) and substituting into (8) yields the scaled equation,

$$\omega t - \frac{\sin 2\omega t}{2} = S^4 \frac{d^2 S}{d(\omega t)^2} + \frac{3}{2} S^3 \left(\frac{dS}{d(\omega t)}\right)^2 + \frac{\rho_0}{\omega^2 \rho B^2} S^3, \tag{9}$$

where $S = \dfrac{R}{B}$ and $B = \left[\dfrac{K R_0^3}{\rho L m_0}, \left(\dfrac{\frac{1}{2} C V_0^2}{\omega^2}\right)\right]^{\frac{1}{5}}$.

For most of the period of interest the term $\dfrac{\rho_0}{\omega^2 \rho B^2} S^3$ is small, and S is a strong function of the scaled time only. Figure 5 shows the measurements of bubble radius growth of Smith (1990) in scaled form and it can be seen that they can be represented as having a common slope. This can be transformed to give the bubble expansion velocity as

$$\frac{dR}{dt} = v = 480\left[\frac{\frac{1}{2} C V_0^2}{\Delta t^3}\right]^{\frac{1}{5}} \text{ m / s}, \tag{10}$$

where the stored energy is in Joules and the half period Δt in microseconds.

The initial radius R_0 defined by equation (7) represents the effect of the early stages of the discharge and is not directly related to a physical dimension. Measurements with different diameter cavities and different initial bubble sizes

showed that the peak pressure produced was independent of these factors. The quantity defined by equation (7) on the other hand plays an essential role in determining the peak pressure.

Although the intercepts R_0 determined from the limited set of radius versus time measurement did not display a discernable trend, it was found that the assumption of a fixed value for the intercept in the scaled coordinate system of equation (9) resulted in the most satisfactory fit to the pressure data. The resulting scaling is as follows:

$$\frac{R_0}{(R_0)_{REF}} = \left[\frac{\frac{1}{2} C V_0^2 \Delta t^2}{\left(\frac{1}{2} C V_0^2 \Delta t^2 \right)_{REF}} \right]^{\frac{1}{5}}, \tag{11}$$

where the reference values have been chosen to match the experimental results for the case of 100 μF, 13 μH with 8 J of stored energy. The resulting reference values for R_0 and Δt are 1.0 mm and 154 μs, respectively.

Equations (2) and (6) can be combined to give the time variation of the pressure as

$$p(\omega t) = K_0 \frac{\frac{1}{2} C V_0^2}{R_0^3} \frac{\left(\omega t - \frac{\sin 2\omega t}{2} \right)}{\left(1 + \frac{v}{R_0 \omega} \omega t \right)^3} + \frac{p_0}{\left(1 + \frac{v}{R_0 \omega} \omega t \right)^3}, \tag{12}$$

where K_0 is an overall constant and v is calculated from equations (10) and (11). K_0 and $(R_0)_{REF}$ are chosen to give an optimum fit to the experimental data.

Pressure measurements were made for a wide range of discharge conditions for a source depth of one metre with a hydrophone positioned approximately 12 cm from the plasma gun exit. To compare these with equation (12), allowance must be made for this offset. Applying (1) with d^2R/dt^2 set to zero (a constant radial expansion velocity), as was assumed in the derivation of (12), yields the reduction factor:

$$\frac{p(r) - p_0}{p(R) - p_0} = \frac{2}{3} \left(\frac{R}{r} \right) \left[2 - \frac{1}{2} \left(\frac{R}{r} \right)^3 \right]. \tag{13}$$

Figure 6 compares the optimized fit of equation (12) for the peak pressure with the experimental values where each point represents the mean of four shots. The fits for the shorter discharge times are good, but at the lowest frequency the fit underestimates the pressure at low energy and overestimates at high energy, suggesting that the efficiency of energy transfer may decrease slightly with increasing energy.

The optimized fitting constants have the following values for an immersion depth of 1 m: $K_0 = 3.2$, $(R_0)_{REF} = 1.0$ mm, $(^1/_2 C V_0^2)_{REF} = 8$ J and $(\Delta t)_{REF} = 154$ μs, and the cavity size is 3 mm diameter, 6 to 8 mm in depth.

The degree to which the theory reproduces the initial pressure pulse is illustrated in Figure 7. This shows the pressure variation relative to ambient pressure for four sets of operating conditions representing the extremes of the ranges investigated, i.e., 100 μF, 13 μH and 200 μF, 51 μH. The peak pressures vary by about ± 15 percent, equivalent to ± 2 dB re 1 μPa at 206 dB.

As an additional check on the model of the initial pressure pulse, a series of measurements were made with the hydrophone positioned at different distances from the source whilst maintaining fixed discharge conditions (100 μF, 51 μH at 600 V). Figure 8 compares the ratio of the peak pressure relative to that at a distance of 8 cm from the source for the optimized theory with the measured values. The reduction in peak pressure with the source-to-hydrophone separation distance is well-represented by the theory. The theory of the primary pressure pulse presented here has been optimised for the energy and frequency ranges of interest by the selection of appropriate matching constants. A similar modelling approach could be applied to spark driven systems in general. In particular, the scaling of the Rayleigh bubble equation

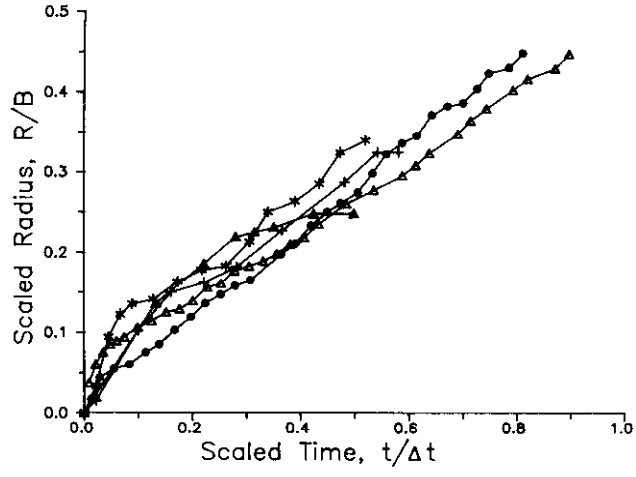

Fig. 5. Expansion of bubble radius with time in scaled coordinates.

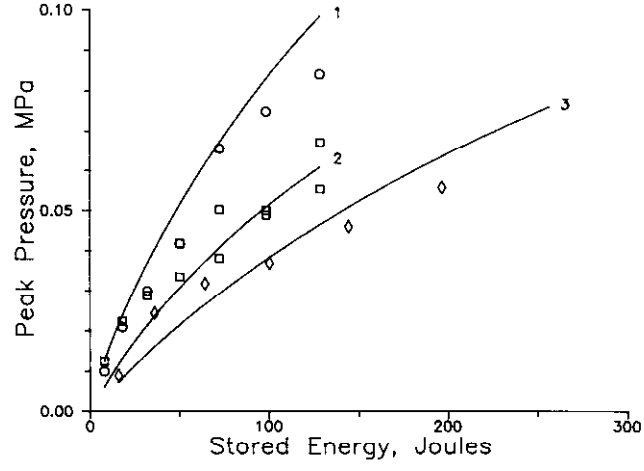

Fig. 6. Comparison between predicted (solid curves) and measured primary pulse peak pressures, hydrophone distance 12 cm. Circuit parameters are: curve 1 - circles, 100 μF, 13 μH; curve 2 - squares, 100 μF, 51 μH; curve 3 - diamonds, 200 μF, 51 μH.

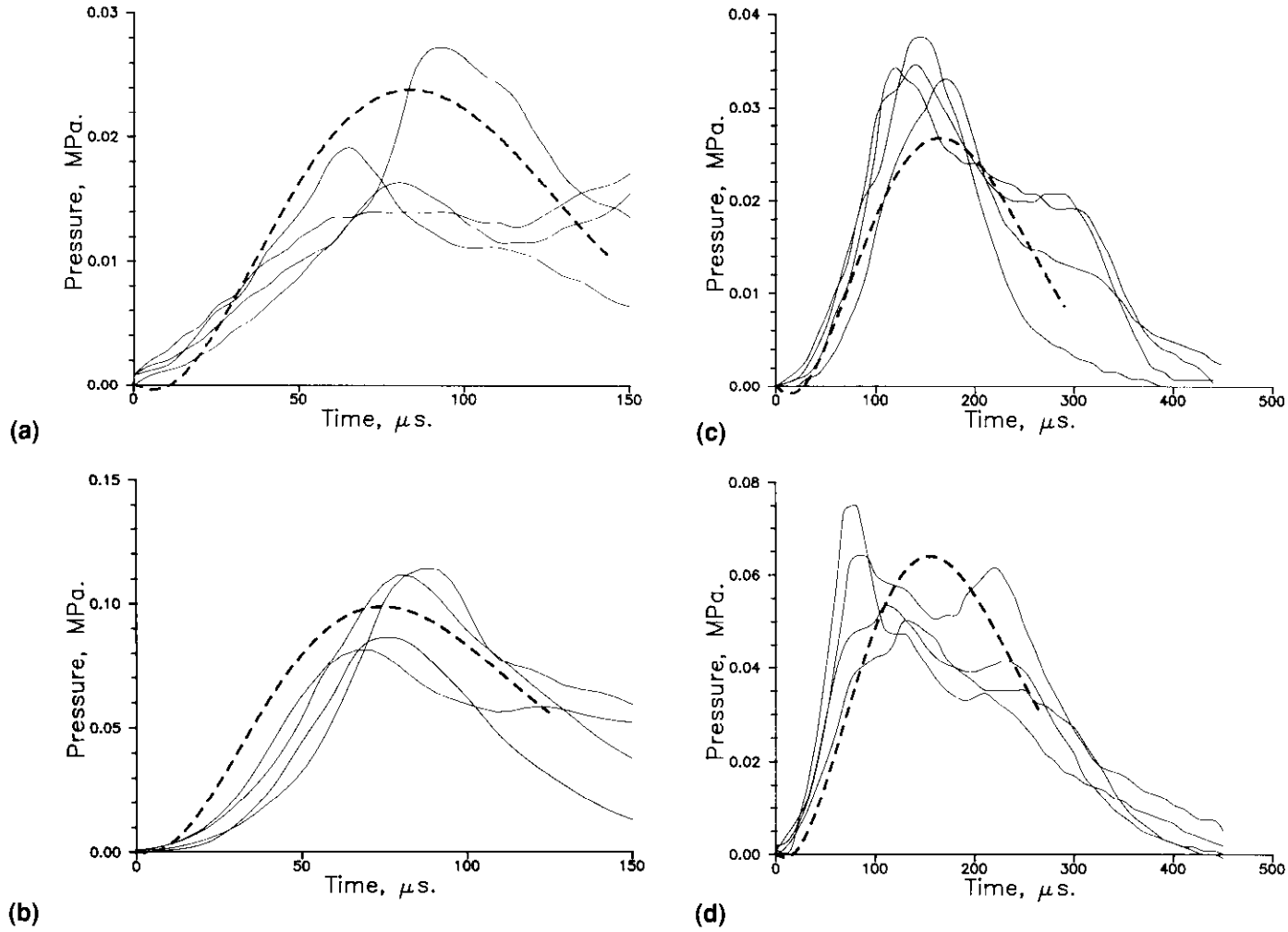

Fig. 7. Comparison between predicted, thick-dashed line and measured primary pressure waves (four repeat shots); thin lines, hydrophone distance 12 cm. Circuit parameters are: **a**) 100 μF, 13 μH, 600 V; **b**) 100 μF, 13 μH, 1600 V; **c**) 200 μF, 51 μH, 800 V; and **d**) 200 μF, 51 μH, 1400 V.

which plays a crucial role in the model could be adapted to other forms of bubble generation.

The Overall Source Characteristics

An inevitable consequence of pressure production from an expanding bubble is the generation of a second pressure pulse during the process of collapse and, in general, a train of pulses of decreasing amplitude results. As noted in the introduction, the plasma jet configuration limits the process to a single coherent collapse and the overall signature consists of a pair of pulses. This is clearly displayed in the record of the plasma jet signature obtained by McGee et al. (1992), although they mistakenly attribute the bubble pulse to a surface ghost.

Attempts to model the bubble pulse with a solution of the differential equation (1) by assuming either an adiabatic or isothermal expansion process failed to produce the observed time delay between the generating pulse and the bubble pulse. Taking as initial conditions the output of the generating pulse model, equation (11), the bubble pulse time is overestimated by approximately 50 percent, and although the dependence on stored energy alone is reproduced, its rate of increase is also overestimated.

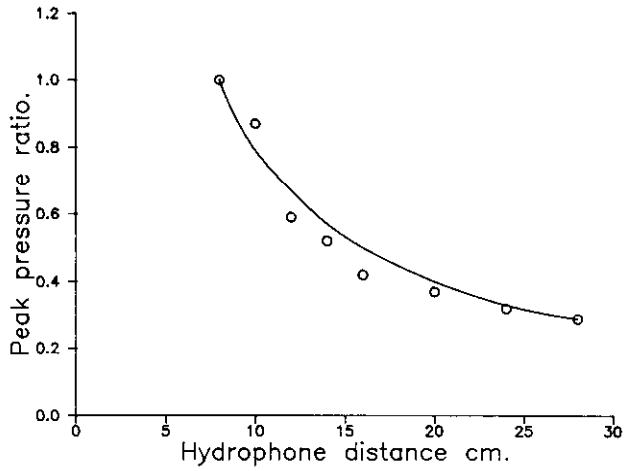

Fig. 8. Peak pressure referenced to 8 cm separation vs. hydrophone distance; theory, thin line, experiment, circles.

The following semiempirical method based on measured bubble behaviour gave a close agreement with measured pressures. The video images (see Figure 2) of the expanding bubbles were measured to determine their radius versus time. A polynomial fit (a quartic) over the time up to the bubble collapse was obtained and the velocity and acceleration determined from the fitted curve.

Figure 9 shows the normalized model pressure calculated from the measured bubble diameter, together with the solution of equation (1), and an experimental normalized pressure trace (both calculated at 1 m) obtained with the same electrical parameters. The bubble period (the time between the two positive pressure peaks) for the experimental measurement was actually 4.2 ms. This was corrected to 4.7 ms because the pressure where the images were taken was at a depth of only a few centimetres while the experimental measurement was made at a depth of 1.2 m. This was done following the work of Arons et al. (1948). Peak pressure predicted by the model was approximately 8.6 kPa while the measured pressure was 12 kPa. This difference is believed to be caused by the nature of the quartic fit to the bubble radius data. Velocity at $t = 0$ for the polynomial function was 34 m/s (with strong deceleration), whereas the streak data yielded a constant expansion velocity of 40 m/s. In addition, the vapour bubble is not spherical and does not possess exactly the same symmetry from experiment to experiment. The rapid decrease in pressure following the first maximum of the experimental pressure is not present on the model pressure signature derived in this way. It is, however, reproduced in the more detailed model of equation (12). The experimental pressure trace is in fact the mean of several shots in order to compare with the independent imaging shot. The bubble pulse is broadened in the averaging process. With all these limitations, the oscillating spherical bubble model still gives a reasonable representation of the pressure production mechanism of the expanding and contracting vapour bubble.

Figure 10 shows the variation of pulse separation with stored energy for the ranges tested. Each point again represents the mean of four shots and they are well-represented by a power law of the form

$$t_p = 1.31\left(\frac{1}{2}CV_0^2\right)^{0.24} \tag{14}$$

This differs from the one-third power law dependence on energy input of the idealised theory which is found experimentally for explosives, Arons et al. (1948), and confirms the slight decrease in energy transfer efficiency with increasing stored energy. Equation (11) can be used to calculate the generating pulse characteristics for various circuit conditions, and Figures 11 and 12 show the variation of peak pressure and the time to attain peak pressure as a function of stored energy for the range of test conditions covered.

A judicious choice of circuit parameters combined with appropriate filtering of the returned echoes allows the user some control over the effective source signature. The width of the generating pulse is dependent on both the stored energy and the circuit discharge frequency, while the bubble

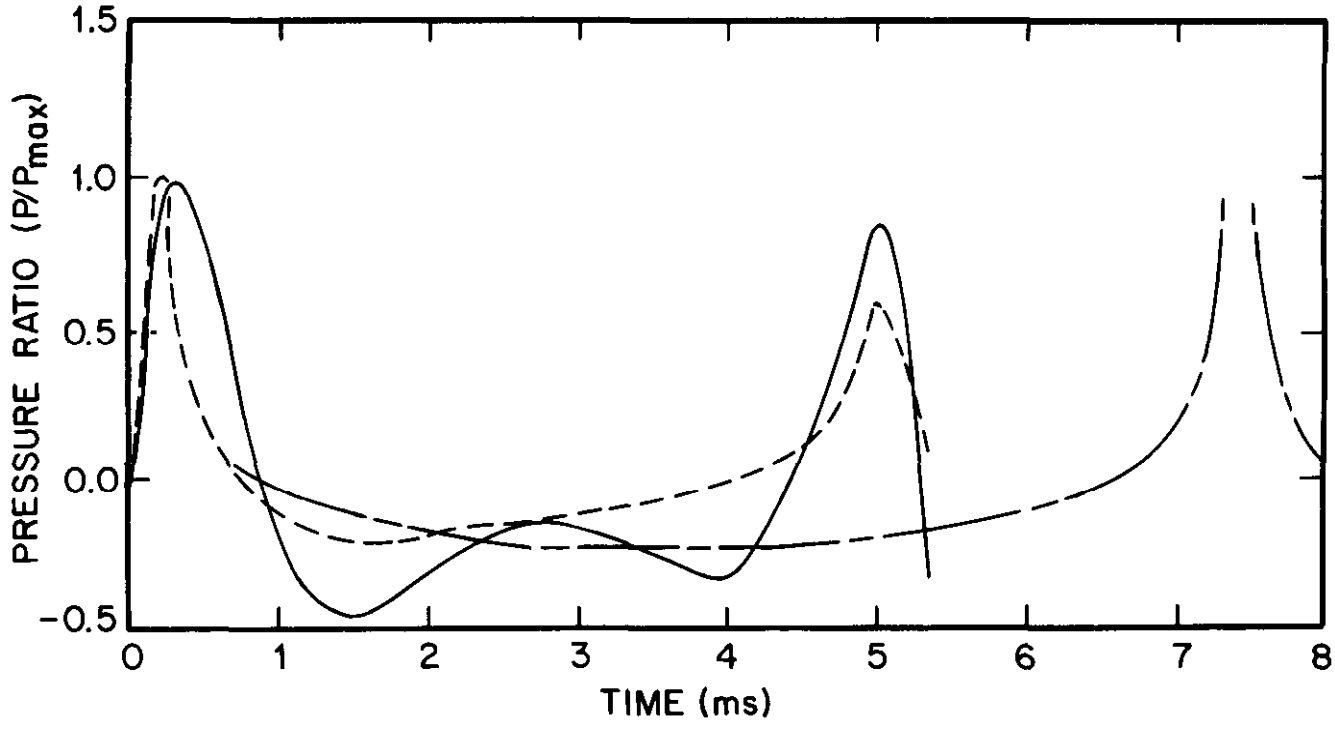

Fig. 9. Comparison of normalized model and experimental results. Dashed curve is experimental, solid curve is semiemperical, and chain dotted curve equation (1).

collapse pulse appears to be of a fixed width of 100 to 150 μs, for the most part irrespective of the circuit conditions. The exception is at the minimum charging voltage of 400 V when the bubble pulse is erratic in form. The separation between the pulses for a fixed immersion depth depends only upon the stored energy. Figure 13 shows examples of pressure signatures corresponding to the extremes of the frequency ranges tested. The lower frequency corresponds to the circuit reported on by McGee et al. (1992). The small scale oscillations between the pulses are the result of reflections within the test facility. They are absent in the record obtained by McGee at al. (1992) in an open environment. For the 100 μF, 13 μH circuit the primary and bubble pulses are approximately equal in amplitude, independent of stored energy.

The above discussions centered on results obtained at small immersion depths, but some potential applications require operations at greater depths with a consequent modification of the source signature. Higher pressures can be expected to modify the electric arc characteristics and hence the energy transfer efficiency. In general, arcs confined in an evaporating environment are subject to local convective flows, and thus higher column voltage gradients and temperatures are to be anticipated at higher pressures, Jones and Fang (1980). For a given energy input, the bubble pulse period is expected to vary as $Z_0^{-5/6}$, where Z_0 is the absolute hydrostatice pressure, while the magnitude of the bubble collapse pressure peak is unchanged, Arons et al. (1948).

As the width of the generating pulse is extended by lowering the discharge frequency, the emphasis can be placed on either pulse by the use of high- or low-pass filters. This is illustrated in Figure 14 which compares the result of applying 33-element long Lanczos cosine digital filters to the 200 μF, 13 μH record of Figure 13. The high-pass filter with 5 kHz cutoff very effectively eliminates the lower frequency generating pulse. At the highest discharge frequency tested, the pulses have similar widths and must be treated as a pair of pulses whose separation can be controlled by the stored energy of the systems. Filtering can then be used to further isolate the common frequency content of the pulses.

The pressure wave transmitted to the underlying structure of interest depends not only upon the source signature but on its convolution with reflections from nearby surfaces. In fact, the tuning of the probing signal by adjustment of the source to free-surface distance is a standard operational practice. The effect of the source-to-surface reflections can be approximately simulated by adding a sign-reversed and attenuated copy of the source signature, delayed by an appropriate reflection time. Due allowance must of course be made for the modification of the signal amplitudes with distance. Examination of equation (1) suggests that the term $(R^2/r^2 \cdot dR/dt)^2$ on the R.H.S. rapidly becomes negligible with increasing distance from the source and the whole pressure pulse then scales uniformly with distance.

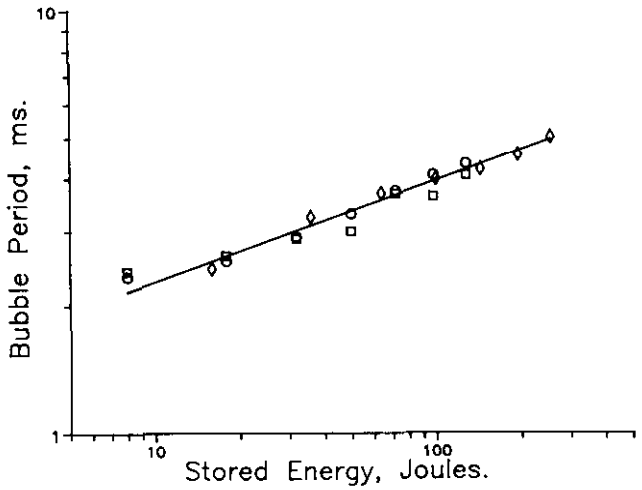

Fig. 10. Bubble period as a function of stored energy. Circuit parameters are: circles 100 μF, 13 μH; squares 100 μF, 51 μH; diamonds 200 μF, 51 μH.

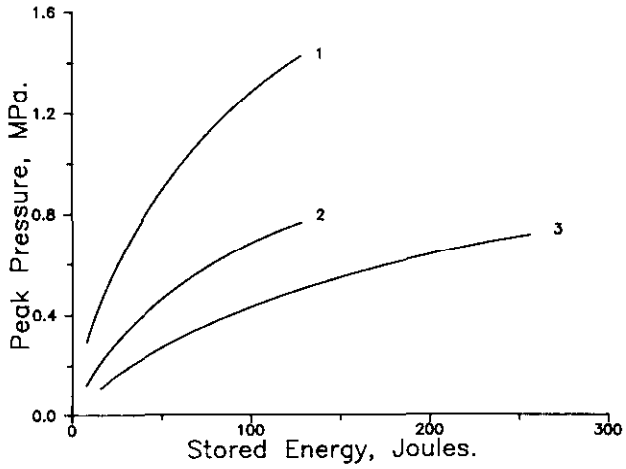

Fig. 11. Peak primary pressure at source vs. stored energy and discharge time. Circuit parameters are: curve 1 - 100 μF, 13 μH; curve 2 - 100 μF, 51 μH; curve 3 - 200 μF, 51 μH.

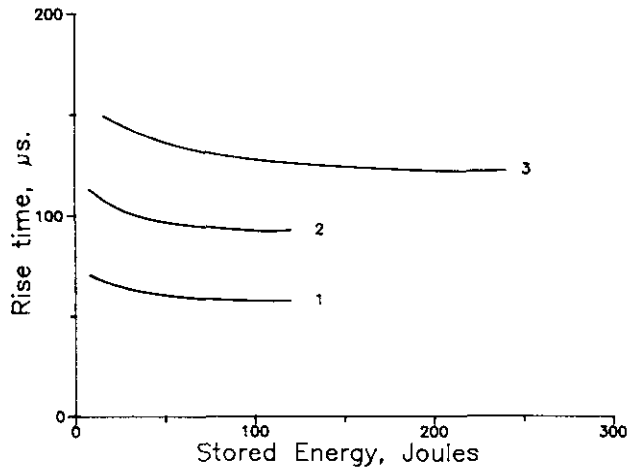

Fig. 12. Rise time of primary pressure pulse vs. stored energy and discharge time. Circuit parameters are: curve 1 - 100 μF, 13 μH; curve 2 - 100 μF, 51 μH; curve 3 - 200 μF, 51 μH.

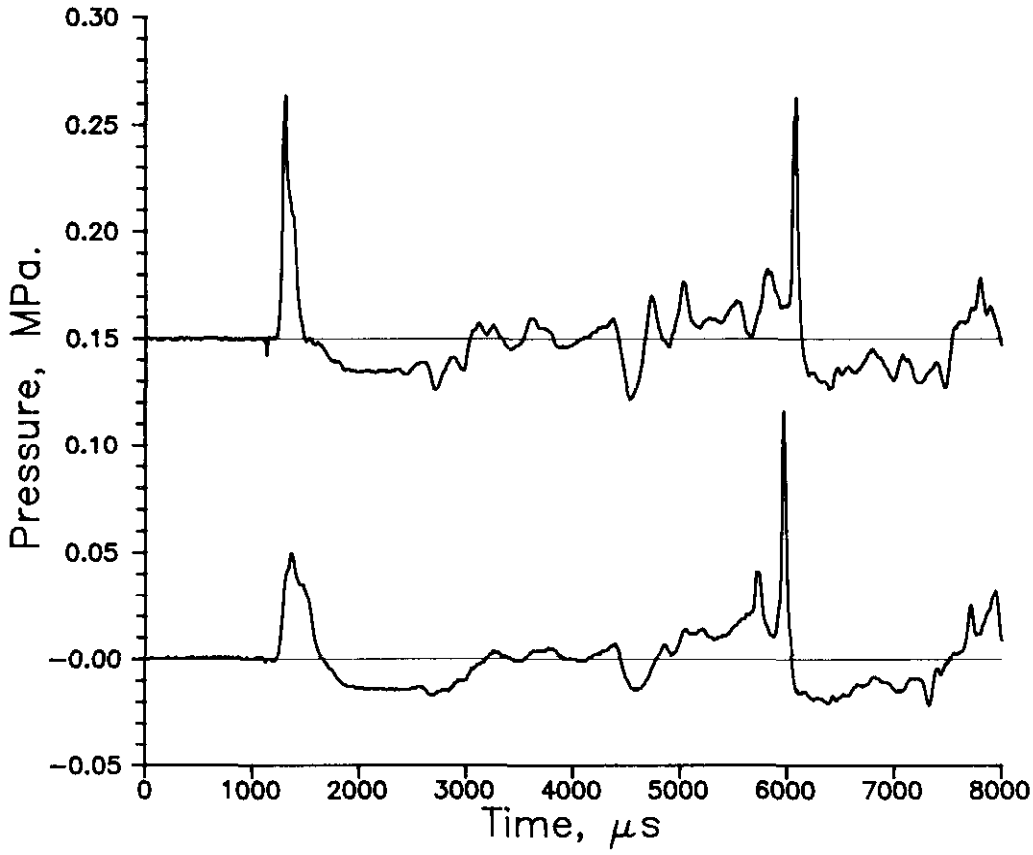

Fig. 13. Complete pressure trace for circuit parameters of 100 μF, 13 μH, 1600 V (upper trace) and 200 μF, 51 μH, 1400 V (lower trace). Note the zero for the upper trace is shifted upward by 0.15 MPa.

Practical Implications

Although the purpose of this paper is to explore the pressure signature produced by the pulsed plasma jet there is always the all-important practical aspect of how this translates into real-life seismic profiling. This is discussed at some length by Smith (1990) and briefly by Pitt et al. (1988). However, for completeness, Figure 15 shows a simultaneous comparison between a pinger source and the plasma jet which was made on Patricia Bay (a bay on the southeast corner of Vancouver Island – the site of the Institute of Ocean Sciences). The pinger was a piezoelectric transducer system operating at 7 kHz and producing 4 "pings" a second, each ping lasting 0.5 ms; input power was 1000 W. The pinger used its own transducer as a receiver while the plasma jet used a 19-element array of Geospace MP-17 hydrophones connected in parallel (active length 6.1 m, bandpass 800 Hz to 20 kHz). The plasma jet stored energy was 150 J and was fired once every two seconds. A comparison of the measured pressure waveform and its Fourier transform for the two sources is shown in Figure 16.

The characteristics of the profiles are quite different. Over these hard bottoms, resolution by the 7 kHz pinger of the upper subbottom is better than the plasma gun but the penetration seen in the plasma gun profile is lacking. Sedimentary layers imaged by the plasma gun under the hilly structure between horizontal positions 0 and 12 are not seen on the pinger profile. Layering seen on the pinger record near horizontal position 18, between the sea floor and the hilly structure, is not imaged well by the plasma gun, although it should be recognized that the receiving systems are quite different in each case. With the frequency and electrical energy differences between the two devices being quite substantial (pinger ≈ 500 J per ping, plasma gun ≈ 150 J per shot), the lesser penetration expected from the higher dominant frequency pinger is somewhat compensated for by the larger energy.

There are other practical ramifications which, although they have not been explored in detail by the authors, are worthy of brief consideration. Because the plasma jet is an electrical discharge its firing time is very precise. Thus, arrays of plasma guns, both in-phase and out-of-phase, could be used to increase the acoustic power for increased bottom penetration or to focus the overall acoustic beam, even though each element of the beam array is isotropic. The plasma gun is quite small; one version is housed in a tube 10 cm in diameter and about 100 cm long (total mass, 14 kg). Thus, its use in restricted areas which are too confined for the use of conventional sources such as boomers is a distinct possibility, for example, tracing buried pipelines across rivers. In fact, it could be lowered down water-filled boreholes and used in conventional land-based seismology and for tomographic imaging of reservoir processes, an application requiring operation at high-ambient pressures.

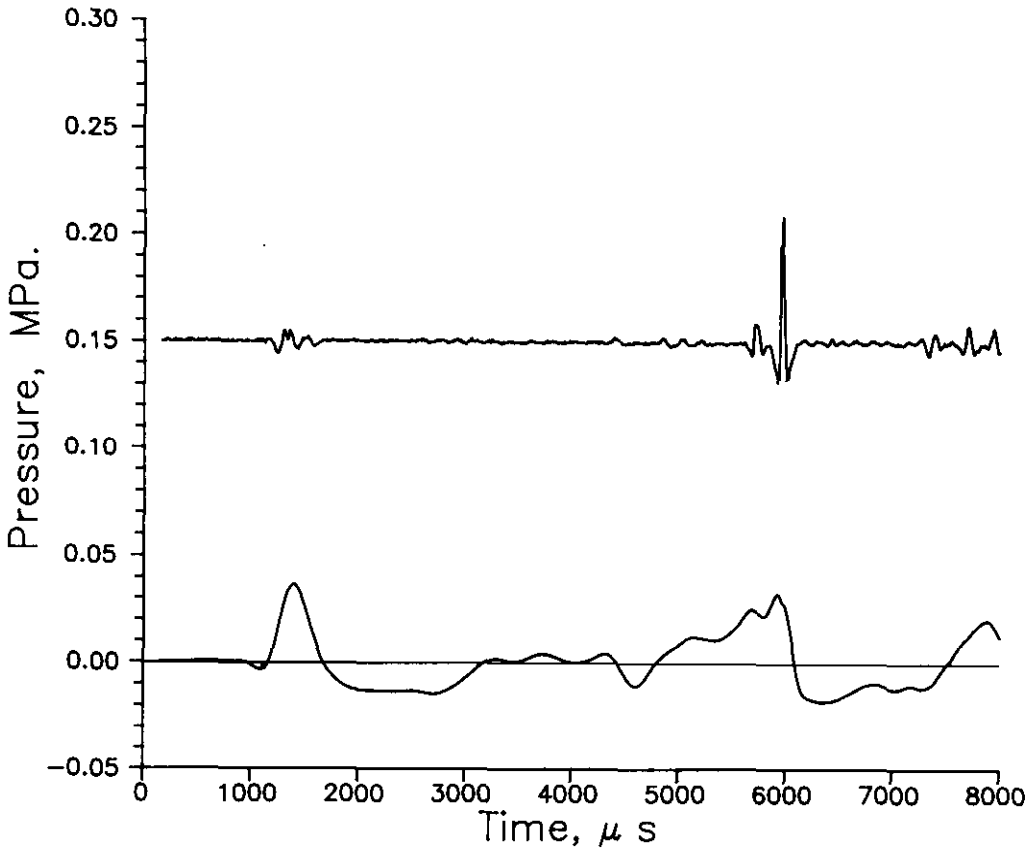

Fig. 14. High- and low-pass filtered versions for 200 μF, 51 μH, 1400 V with cutoff frequencies of 5 kHz (upper trace) and upper cutoff frequency of 830 Hz (lower trace). Note the zero for the upper trace is shifted upward by 0.15 MPa.

Conclusions

Reasonable agreement between the theoretical model and experiment indicates that the pressure-producing mechanism of the underwater discharge of the plasma jet is the rapidly expanding vapour bubble, in many ways similar to a small underwater explosion. Control of the duration of the primary pressure pulse, the time the pressure is above ambient from the initial discharge, can be controlled by the electrical circuit parameters (capacitance and inductance). The maximum pressure values depends on the square of the peak discharge current; this, too, is controlled by the circuit parameters and additionally by the applied voltage. For a fixed-source depth, the bubble period depends only on the total stored electrical energy. The statistical variation in the peak pressure is equivalent to ± 2 dB re 1 μPa at 206 db.

References

Arons, A.B., Slifko, J.P. and Carter, A., 1948, Secondary pressure pulses due to gas globe oscillation in underwater explosions: I. Selection of adiabatic parameters in the theory of oscillation: J. Acoust. Soc. Am. **20**, 271-276.

Arsentev, V.V., 1965, On the theory of pulse discharge in a liquid: J. Appl. Mech. and Tech. Phys. **5**, 34-37.

Cole, R.H., 1948, Underwater explosions: Princeton Univ. Press.

Cowley, M.D., 1974, Integral methods of analysing electric arc: I. Formulation: J. Phys. D: Appl. Phys. **7**, 2218-2232.

Jones, G.R. and Fang, M.T.C., 1980, Physics of high-pressure areas: Reports on Progress in Physics **43**, 1415-1465.

Keller, J.B. and Kolodner, I.I., 1956, Damping of underwater bubble oscillations: J. Appl. Phys. **27**, 1152-1161.

Lamb, H., 1945, Hydrodynamics: Dover Publ. Inc.

McGee, T., Davis, A., Anderson, H. and Verbeek, N., 1992, High-resolution marine seismic source signatures: Presented at the European Conference on Underwater Acoustics, Luxembourg.

Pitt, P.L., Smith, R.D., Sheffler, G.C. Warren, R.D., Clements, R.M. and Hamilton, T.S., 1988, A pulsed plasma jet acoustic source for profiling the ocean floor: Geophys. Prosp. **36**, 523-536.

Smith, R.D., 1990, An investigation of the plasma jet as an underwater acoustic source: Ph.D. thesis, Univ. of Victoria.

_____, Pitt, P.L., Ridley, J.D., Sheffler, G.C. and Clements, R.M., 1987, Underwater sound from a pulsed plasma jet: Acoust. Lett. **10**, 161-165.

Stewart, D.B. and Baird, J.P., 1980, Laser interferometer probe for underwater pulse from electric arc: Acoust. Lett. **4**, 58-64.

Topham, D.R., 1971, The electric arc in constant pressure axial gas flow: J. Phys. D: Appl. Phys. **4**, 1114-1125.

_____, 1972, The characteristics of axial flow electric arcs subject to pressure gradients: J. Phys. D: Appl. Phys. **5**, 533-541.

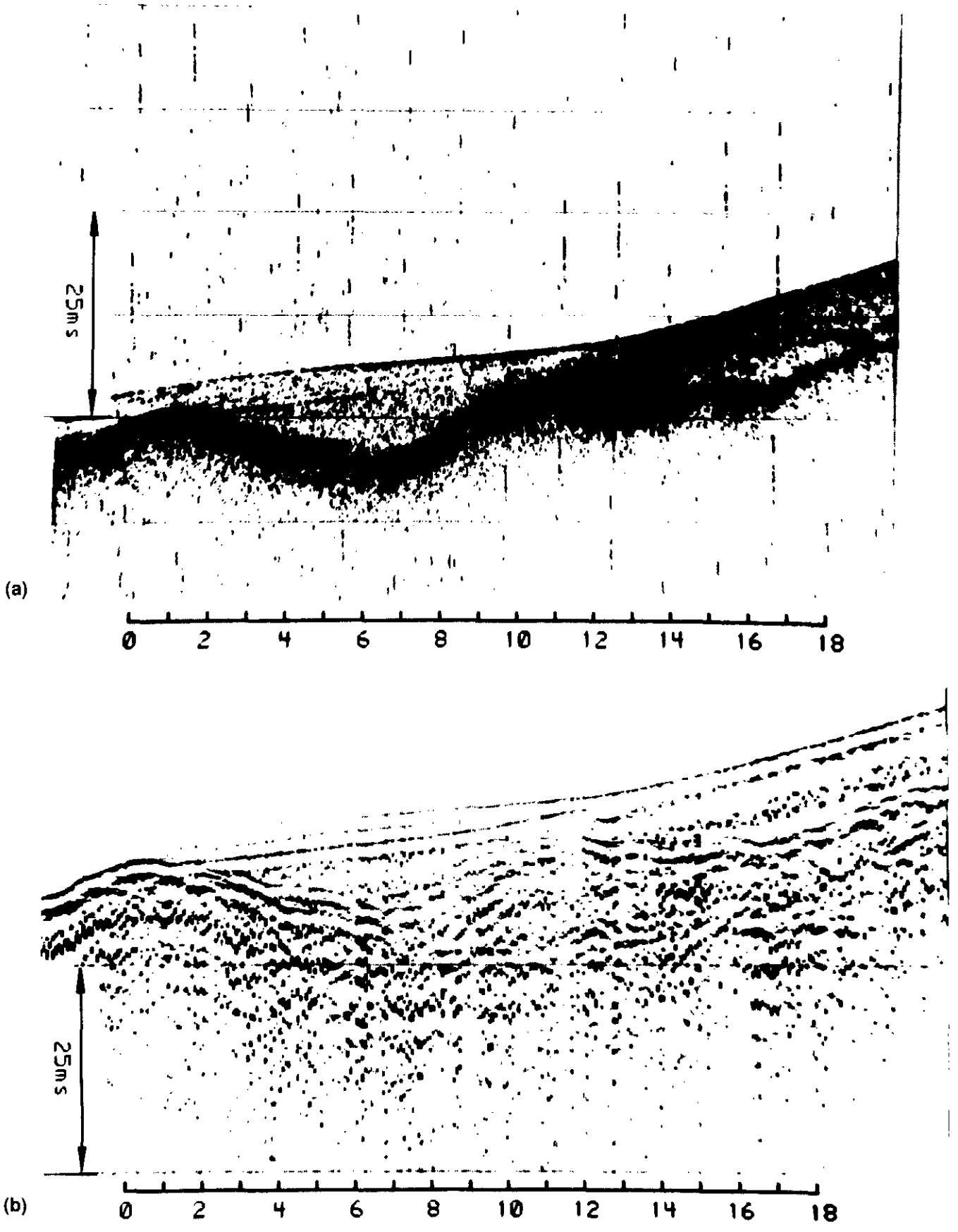

Fig. 15. Subbottom profile of Patricia Bay. **a)** pinger, **b)** plasma gun. The horizontal distance depicted in the figure is about 60 m.

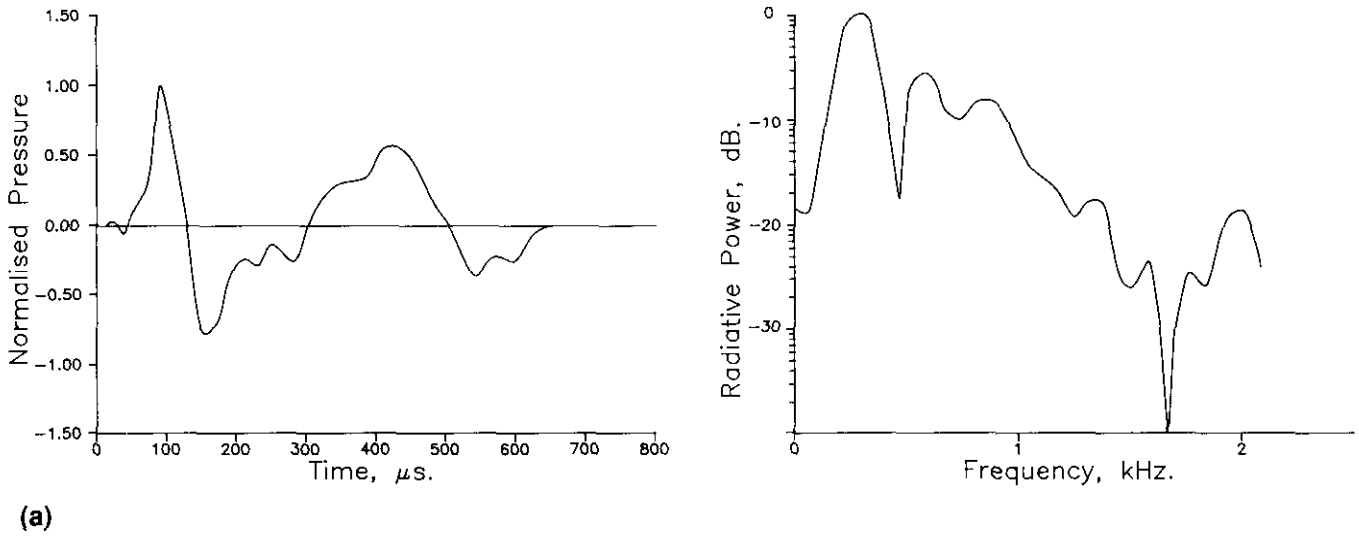

(a)

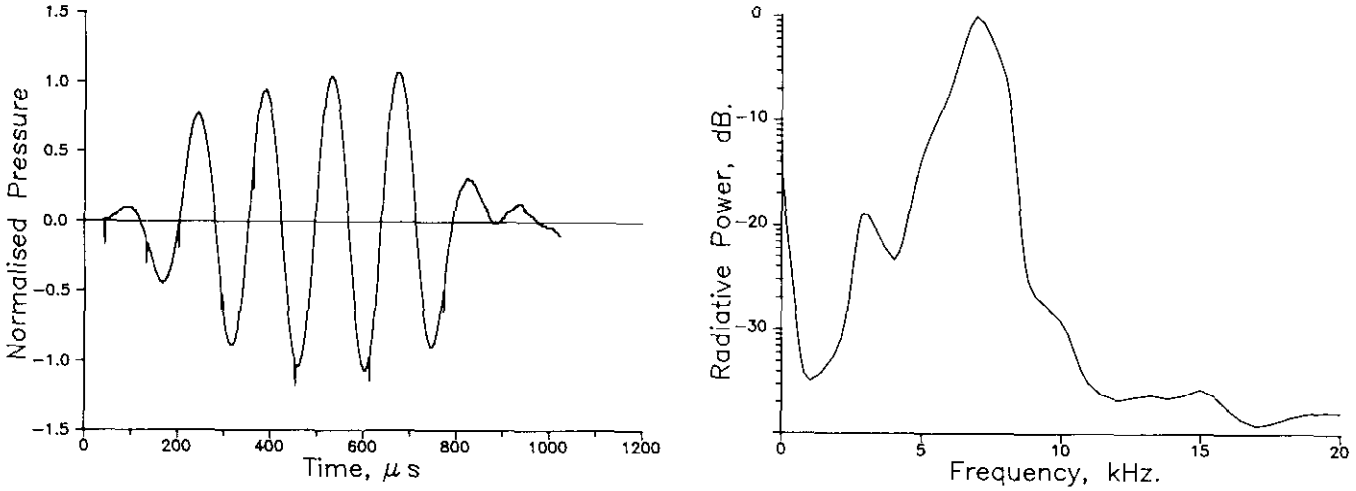

(b)

Fig. 16. Comparison between the output pressure pulse and its Fourier transform for **a)** plasma gun (200 μF, 51 μH, 1200 V) and **b)** pinger.